A QUANTITATIVE ASSESSMENT OF COMPUTATIONAL RESULTS FOR BEHIND ARMOR DEBRIS

G. R. Johnson[1], R. A. Stryk[1], C. A. Gerlach[1], T. J. Holmquist[1] and N. L. Rowe[1]

[1]*Network Computing Services Inc., P. O. Box 581459, Minneapolis, MN 55458, U.S.A.*

This article presents a quantitative assessment of computational results for Behind Armor Debris (BAD). Comparisons are made to experimental data, and parameters are varied to determine the effects of material strength, material ductility, grid size, particle smoothing distance, and postprocessing options. The computations are based on a Lagrangian approach that begins with finite elements and then converts the highly distorted elements into meshless particles as the solution progresses. The particles have variable nodal connectivity and can readily handle high distortions. Because both the elements and particles are Lagrangian they do not lose definition as they travel through large spaces.

INTRODUCTION

When a projectile perforates a target there are often fragments of material (from both the projectile and the target) that are formed behind the target. This is generally referred to as Behind Armor Debris (BAD). The BAD consists of fragments of different materials, sizes, shapes, masses and velocities. It is desirable to characterize this BAD in an accurate manner to predict damage to components behind the target. Although there has been much experimental research and some computational research directed at characterizing the BAD, this remains a challenging problem.

Recently Johnson and Stryk [1] presented some computations of BAD that showed qualitative agreement with experimental data from x-rays of the debris field. These computations were performed with a Lagrangian approach that included both finite elements and meshless particles [2]. For this approach the initial grid consists entirely of Lagrangian finite elements. Then, as the computation progresses and some of the elements become highly distorted, they are automatically converted into (Lagrangian) meshless particles. These meshless particles can represent very severe distortions because the particles have variable nodal connectivity (each particle node can acquire new neighbor particles during the course of the computation). Because the particles are Lagrangian, they do not lose definition as they travel through large air spaces. Another recent study has been performed using an Eulerian computational approach [3].

DESCRIPTION OF COMPUTATIONAL APPROACH

Figure 1 shows a finite element grid with three elements on the surface (A, B, C) that are designated as candidates for conversion to meshless particles. An element is converted to a particle when the element has at least one side on the surface and the equivalent strain exceeds a user-specified value. All of the converted element variables are transferred to the new particle node, the element is removed from the computation, and the contact surfaces for the remaining elements are updated. The particle is then attached to the adjacent element face until the element containing the face is converted to a particle. In addition, at other interfaces it is possible for the standard (finite element) nodes and the particle nodes to contact and slide along the external surfaces of the finite elements. An algorithm for particle nodes of different materials contacting one another is also included. The computations are performed with the EPIC code and the Generalized Particle Algorithm is used for the meshless particles [2,4].
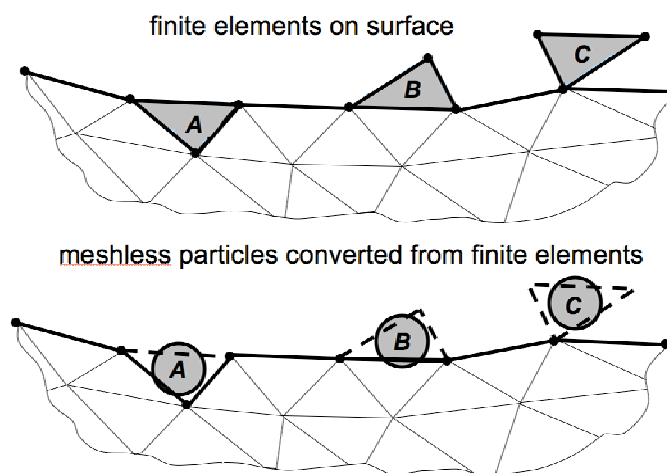
Figure 1. Conversion of finite elements into meshless particles

Figure 2 shows a group of elements and particles that form a fragment. An element can only be converted to a particle when it is on the surface and when the equivalent plastic strain has exceeded a user-specified value of about 0.3 to 0.5. As a fragment begins to form, the localization of strains around its surface can occur in intact material during the dynamic response, rapidly in failed material that has no strength, and (unfortunately) between particles that have not failed but have separated beyond the smoothing distance (usually 1.5 to 2.0 particle diameters). The authors have not observed a significant problem with this numerical localization because the material generally fails before the smoothing distances are exceeded. In fact, for many lower-ductility materials the material fails before the element is converted into a particle.

fragment composed of elements and particles

full bond

half bond

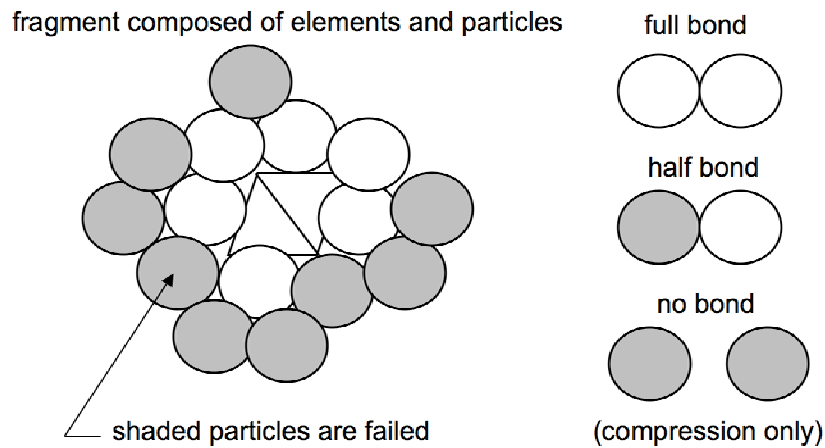no bond

shaded particles are failed

(compression only)

Figure 2. Characteristics of material failure and fragmentation

The right side of Figure 2 shows the three possible combinations of adjacent particles: two unfailed particles (designated full bond), one unfailed particle and one failed particle (designated half bond), and two failed particles (designated no bond). Unfailed particles can develop both tension and shear stresses that tend to keep the particles from separating. The stresses within each particle lead to equal and opposite forces between the particles. If one particle is failed and the other is not (half bond) then the failed particle cannot contribute any attractive forces between the two particles, but the unfailed particle can. Therefore it is possible for an unfailed particle to stick to a failed particle. If both particles are failed (no bond) then they can only develop compression (repulsive) forces between the two. Failed particles behave like a liquid. They can develop compressive stresses but cannot develop tensile or shear stresses. Therefore, it is not possible to form a fragment that is composed of only failed particles.

After the computation has been performed it is possible to determine the distribution of fragments by postprocessing. Currently it is possible to determine the number of fragments that are formed in various ranges of mass, size, kinetic energy and momenta (along any user specified direction). There are two user-supplied input parameters that must be used for the postprocessing. The first is the minimum number of elements and particles (N) that are required to form a fragment. If $N = 1$ then every single particle could be counted as a fragment and there could be many small fragments. Also, it is not possible to determine any fragment sizes that are smaller than the size of the elements and particles. If it is desired to determine the sizes of fragments smaller than the elements and particles, then the numerical implementation [5] of the Grady algorithm [6] could be used. For most applications these small fragments are not of interest and the distribution of larger fragments is independent of N (for small values of N that are less than the number of fragments/particles in the smallest fragment of interest).

The second input parameter is a dimensionless distance (α) that is used to determine if two adjacent particles are a part of the same fragment. If $d_{ij} \leq \alpha \overline{D}_{ij}$ then particles i and j are a part of the same fragment. The distance between the centers of the particles is d_{ij} and the average diameter of the two particles is $\overline{D}_{ij}$. If the check is made between a particle and an element then an effective diameter is used for the element. If the check is made between two elements then they must share a common node to be included in the fragment. As this distance check is made between all particles and elements, it is necessary that the computation be carried out to a time sufficient for the fragments to have adequately separated from each other. After an adequate time has been achieved the distribution of fragments is independent of this distance (for $\alpha \approx 2.0$).

COMPUTED RESULTS AND COMPARISON TO EXPERIMENTAL RESULTS

Figure 3 shows a computation of a tungsten-alloy projectile ($l = 68$ *mm*, $d = 17$ *mm*, $M = 212$ *g*, $V = 1020$ *m/s*) impacting and perforating a 25.4 *mm* steel armor plate. This problem was selected because there are experimental data available for comparisons [3]. The Johnson-Cook strength [7] and failure [8] models were used to represent the materials. The tungsten material was well defined and characterized, but the steel material was not specifically defined in the documentation of the experimental results [3]. This baseline computation was performed using 4340 steel with a hardness of $R_c = 30$ [7]. It can be seen that there are many fragments formed from multiple elements and particles, including some large, lower-velocity fragments that are formed from the rear surface of the target around the outer portion of the hole. Although damage contours are not included in this article, most of the fragments have highly damaged (failed) particles on their outer surfaces. There are also many single particles that are failed and are not a part of any fragment.

This computation contains 777,504 elements (for half of the geometry using a plane of symmetry), and the average volume of the tetrahedral elements used in the projectile and the center portion of the plate is about 0.12 *mm*^{3}. For the steel, each element has a mass of about 0.001 *g*, which means there are about 50 elements/particles in a small 0.05 *g* fragment and about 1000 elements/particles in a 1.0 *g* fragment. This computation required 11.5 *hours* (wall-clock) using 8 processors on a Cray XT3.

Figure 4 provides distributions of fragment masses for two experiments and several computations. For a specific fragment mass (on the horizontal axis) the vertical axis shows the number of fragments that have masses greater than the specific fragment mass. For example, the experimental data indicate that there are 22 (experiment #1) and 28 fragments (experiment # 2) with fragment masses greater than 0.5 *g*.
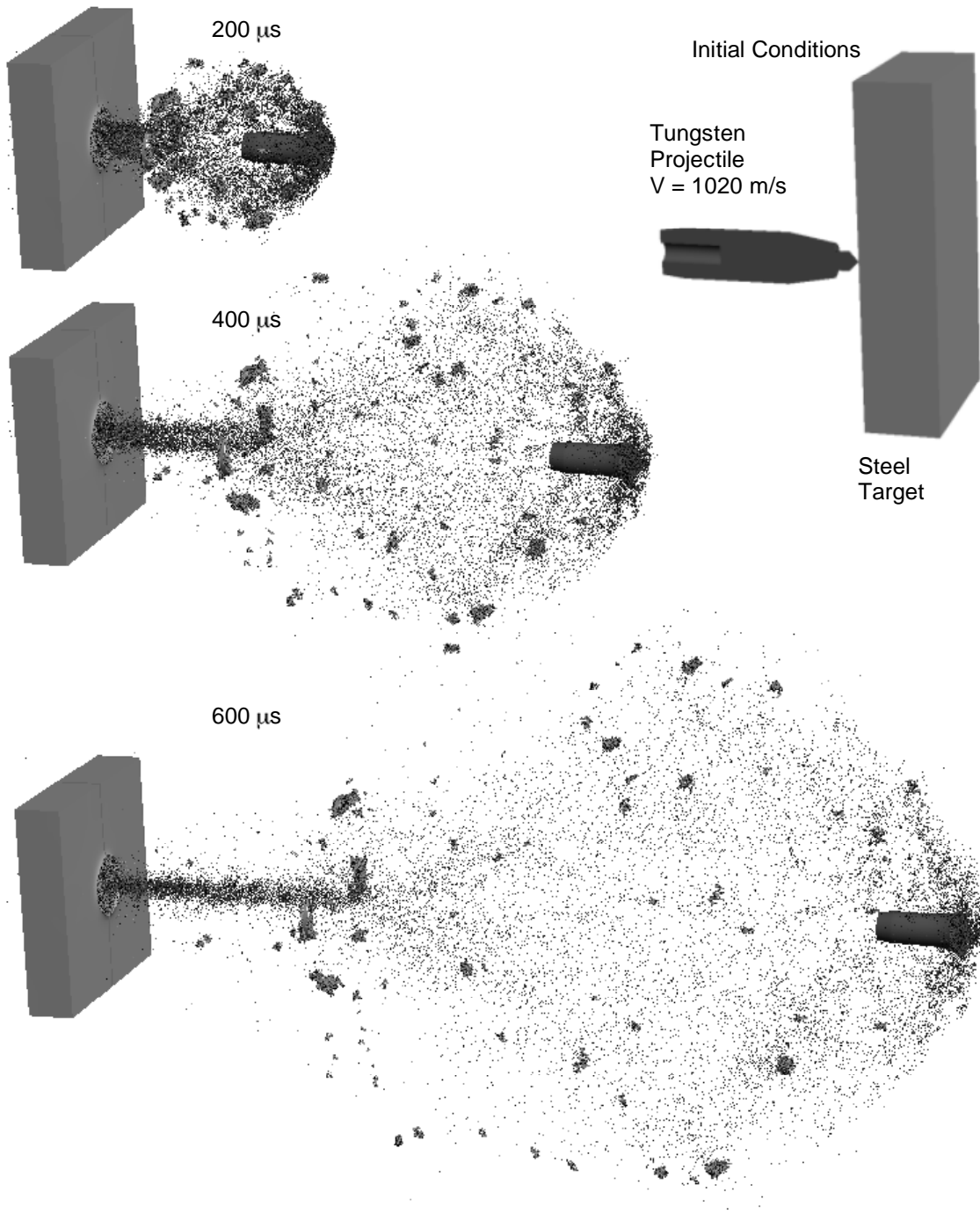
200 μs

Initial Conditions

Tungsten
Projectile
V = 1020 m/s

400 μs

Steel
Target

600 μs

Figure 3. Baseline computation of a tungsten projectile impacting a steel plate at 1020 *m/s*

The baseline computation provides results that are in good agreement with the experimental results (for $m > 0.05$ g), although the computed results have more small fragments and fewer large fragments. A cut-off velocity of 10 percent of the impact velocity was used to eliminate the target as a large fragment. The postprocessing used $N = 4$ and $\alpha = 2.0$, but the results on Figure 4 are not sensitive to these input parameters (because the fragments included in Figure 4 have numerous elements/particles). Also, nearly identical results are obtained if the postprocessing is performed at an earlier time of 200 μs or the final time of 600 μs. This is encouraging as no adjustable input parameters are required to get this good agreement with experimental data.

Recall that the steel armor plate was not specifically defined, so some of the disagreements between experiments and computations may be due to the use of assumed material properties for the steel plate. Additional computational results in Figure 4 show sensitivities to material strength and ductility. For increased strength (applied to the target material only) the yield and strain hardening constants (A and B) in the Johnson-Cook strength model [7] were increased by 50 percent, and for increased ductility three failure-strain constants (D_1, D_2 and ε^f_{min}) in the Johnson-Cook failure model [8] were increased by 50 percent. The results in Figure 4 show the increased strength and ductility produce fewer small fragments.
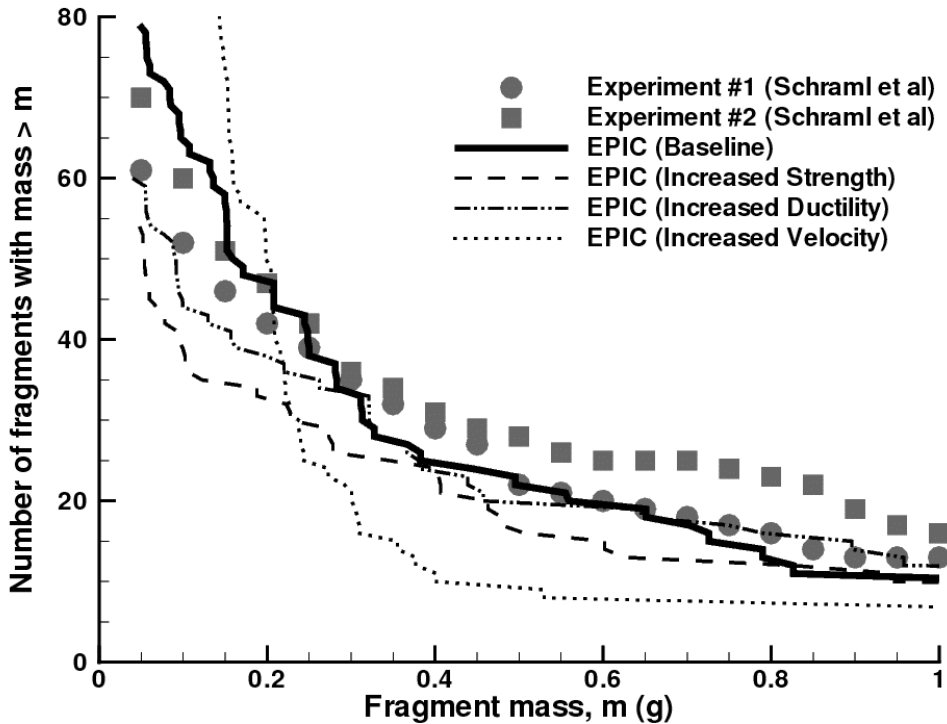

Figure 4. Number of fragments with mass $> m$, versus fragment mass, m

Results of a computation with an increased impact velocity of 50 percent (from 1020 to 1530 *m/s*) are also shown in Figure 4. Here there is a substantial difference, with many more fragments smaller than 0.5 *g* and significantly fewer fragments larger than 0.5 *g*. This is consistent with Grady's model [6], which indicates that the sizes of the fragments are inversely proportional to the strain rates. The higher impact velocity produces higher strain rates, which in turn produce smaller fragments.

The same data are shown in bar graph form in Figure 5. Here the actual numbers of fragments in specific size categories can be seen more clearly. Again there is good general agreement between the experimental data and the computational results. Effects of two numerical parameters are also shown in Figure 5, where the coarse-grid results are for an initial grid that has 164,352 tetrahedral elements (reduced from 777,504) and the smaller-smoothing-distance results are for a smoothing distance of 1.6 particle diameters (compared to 2.0 particle diameters for the baseline computations). Again the results are not significantly different, except that the coarse-grid results provide fewer small fragments and more large fragments.
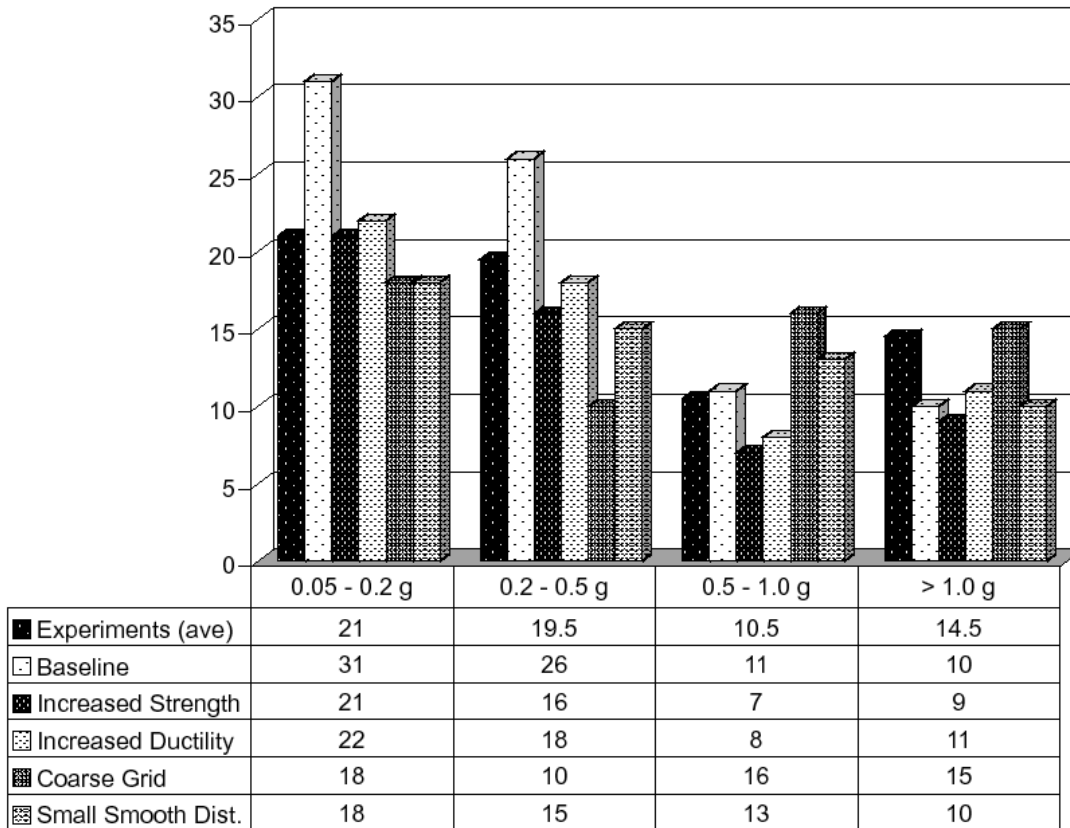

	0.05 - 0.2 g	0.2 - 0.5 g	0.5 - 1.0 g	> 1.0 g
■ Experiments (ave)	21	19.5	10.5	14.5
▫ Baseline	31	26	11	10
▨ Increased Strength	21	16	7	9
▨ Increased Ductility	22	18	8	11
▨ Coarse Grid	18	10	16	15
▨ Small Smooth Dist.	18	15	13	10

Figure 5. Number of fragments in various ranges of fragment sizes

SUMMARY AND CONCLUSIONS

Computations have been performed to obtain a quantitative assessment of BAD fragment sizes, and these results have been shown to be in good agreement with experimental data. The computations were performed with the Lagrangian EPIC code using an algorithm that converts highly distorted elements into particles. The fragment size distributions are only mildly dependent on material strength and ductility variations, but they are very sensitive to impact velocity.

ACKNOWLEDGEMENTS

REFERENCES

1. G. R. Johnson, R. A. Stryk, Behind armor debris computations with finite elements and meshless particles, *22nd International Symposium on Ballistics*, 984-821 (2005).
2. G. R. Johnson, R. A. Stryk, Conversion of 3D distorted particles during dynamic deformation, *Int. J. Impact Eng.,* **28**, 947-966 (2003).
3. S. J. Schraml, H. W. Meyer, D. S. Kleponis, K. D. Kimsey, Simulating the formation and evolution of behind armor debris fields, U. S. Army Research Laboratory report ARL-RP-109 (2005).
4. G. R. Johnson, S. R. Beissel, R. A. Stryk, An improved generalized particle algorithm that includes boundaries and interfaces, *Int. J. Numer. Meth. Eng*., **53**, 875-904 (2002).
5. G. R. Johnson, R. A. Stryk, T. J. Holmquist, O. A. Souka, Recent EPIC code developments for high velocity impact: 3D element arrangements and 2D fragment distributions, *Int. J. Impact Eng.,* **10**, 281-294 (1990).
6. D. E. Grady, Fragmentation of rapidly expanding jets and sheets, *Int. J. Impact Eng.,* **5**, 285-292 (1987).
7. G. R. Johnson, W. H. Cook, A constitutive model and data for metals subjected to large strains, high strain rates and high temperatures, *7th International Symposium on Ballistics*, 541-547 (1983).
8. G. R. Johnson, W. H. Cook, Fracture characteristics of three metals subjected to various strains, strain rates, temperatures and pressures, *Eng. Fract. Mech.*, **21**, 31-48 (1985).